Solar Energy 241 (2022) 24–38

Contents lists available at ScienceDirect

Solar Energy

journal homepage: www.elsevier.com/locate/solener

Analytic function for heliostat flux mapping with astigmatism and defocus

Alberto Sánchez-González

Energy Systems Engineering Group (ISE), Department of Thermal and Fluids Engineering, Universidad Carlos III de Madrid, Av. Universidad, 30, 28911, Leganés, Madrid, Spain

ARTICLE INFO

Keywords:
Convolution
Off-axis aberrations
Tangential and sagittal focus
Concentration ratio

ABSTRACT

Off-axis incidence is inherent to sun tracking mirrors, named heliostats. Moreover, heliostat defocus takes place, provided that the focal length of the mirrors usually differs from their distance to the target. Defocus, along with high incidence angles, lead to astigmatic aberrations, that are overlooked by analytic functions based on convolution. This paper presents an analytic function on the image plane that reproduces these aberrations. As the reflection of the heliostat axes is non-orthogonal with defocus, the identification of the reflected axes plays a key role in the resulting model. In comparison with Monte Carlo Ray-Tracing, the model shows correlation coefficients above 90%, except at the tangential and sagittal foci, where the analytic function is indeterminate. An astigmatic parameter is provided to assess the model validity, which is complementary to UNIZAR at high incidence angles.

1. Introduction

In Solar Power Tower (SPT) plants, thousands of mirrors –heliostats– track the sun and concentrate solar radiation into a central receiver atop a tower. The incidence of sunrays on the mirror is not normal, which leads to off-axis aberrations or astigmatism (Hénault, 2015). As a consequence, the spot size on the target increases, as well as spillage losses (Igel and Hughes, 1979).

To minimize the effect of astigmatism, some heliostat designs have been proposed. In contrast to the widely spread azimuth-elevation tracking heliostats, spinning-elevation –or target-aligned– heliostats attenuate slightly off-axis aberrations because tangential and sagittal planes keep fixed with respect to the reflector (Zaibel et al., 1995; Chen et al., 2004; Lim et al., 2016).

Along with astigmatism, defocus is another issue inherent to heliostats. Because of fabrication constraints, the curvature of the mirror facets is restricted to a limited set in commercial heliostat fields (Buck and Teufel, 2009; Meng et al., 2013; Landman et al., 2016). As mirror focal lengths hardly match the heliostat slant ranges, defocus phenomena take place in the flux distributions.

The accurate mapping of heliostat flux distribution on the receiver is crucial in the design and operation of SPT plants. Real-time optimization of aiming strategies (Sánchez-González et al., 2017; Speetzen and Richter, 2021), field and receiver control (Camacho et al., 2012), and optimization of heliostat fields (Cruz et al., 2017) are examples of tasks that demand fast and accurate tools.

Flux mapping approaches can be classified into two categories: Monte Carlo Ray-Tracing (MCRT) and convolution (Garcia et al., 2008). The MCRT technique traces a bundle of rays from the sun. The convolution approach leads to analytic functions that result from the superposition of error cones, mainly sunshape and concentration. By definition, flux mapping based on convolution is faster than MCRT. On the contrary, aberrations are generally disregarded by the analytic functions.

Widely known models based on the convolution approach are HFLCAL, DELSOL, and UNIZAR. HFLCAL is the only analytic function that includes a term for the astigmatic error (Schwarzbözl et al., 2009). However, because of its strictly circular Gaussian definition, HFLCAL just leads to circular distributions that are inappropriate for rectangular and defocused heliostats. DELSOL uses a Hermite polynomial expansion that takes into account neither astigmatism nor defocus (Walzel et al., 1977). UNIZAR analytic function is based on the error function (Collado et al., 1986), and has shown high accuracy in rectangular focused heliostats with off-axis incidence (Sánchez-González and Santana, 2015).

This paper aims to develop a flux mapping model that reproduces the aberrations due to heliostat defocus and astigmatism. The astigmatic theory will be integrated into an existing analytic function, UNIZAR precisely. As a result, an analytic function will be proposed and tested for single heliostats depending on their position, incidence angle, and defocus. The goal is to improve the accuracy of a fast convolution

E-mail address: asgonzal@ing.uc3m.es.

https://doi.org/10.1016/j.solener.2022.05.045
Received 29 July 2021; Received in revised form 20 April 2022; Accepted 23 May 2022
Available online 7 June 2022

Nomenclature

A	Surface area [m^2]
ah, aw	Limits of the convolution integral [m]
C	Concentration ratio of flux density [–]
D	Slant range, mirror-to-target distance [m]
F	Flux density [W/m^2]
f	Mirror focal length [m]
I_d	Direct normal irradiation [W/m^2]
$\mathbf{H}$	Position vector of heliostat horizontal axis
$\mathcal{H}$	Function based on the Gaussian error function
J	Jacobian of the conformal transformation [–]
L	Mirror characteristic length [m]
LH, LW	Mirror height and width [m]
l	Image length reflected by the mirror [m]
lh, lw	Mirror height and width on the image plane [m]
N	Number of elements
$\mathbf{n}$	Normal unit vector
$\mathbf{O}$	Position vector of mirror center of curvature
R	Mirror curvature radius [m]
Rot	Rotation matrix
$\mathbf{r}$	Reflected unit vector
$\mathbf{s}$	Sun unit vector
$\mathbf{V}$	Position vector of heliostat vertical axis
X, Y, Z	Cartesian coordinate axes
x, y, z	Coordinates in X, Y, Z directions [m]

Greek symbols

α	Azimuth angle [rad], [deg]
β	Angle between sagittal and horizontal axes at image plane [rad], [deg]
δ	Relative distance to circle of least confusion [–]
ϵ	Elevation angle [rad], [deg]
η	Optical loss factor [–]
θ	Rotation angle at image plane [rad], [deg]
ξ, ζ	Linear transformation of x, y [m]
ρ	Cross-correlation coefficient [–]
σ	Error, standard deviation [mrad]
ω	Incidence angle [rad], [deg]

Subscripts

at	Atmospheric attenuation
e	Effective
h	Heliostat
m	Mirror
mod	Model
n	Normal direction
r	Reflection direction
ref	Reflectivity
s	Sagittal
sb	Shading and blocking
sg	Global system of coordinates
sh	Heliostat system of coordinates
si	Image plane system of coordinates
slp	Mirror slope
st	SolTrace
sun	Sunshape
t	Tangential
trk	Tracking
uz	UNIZAR

Accent symbols

$\hat{}$	Non-dimensional length relative to LH
$'$	Reflection, non-orthogonal

Acronyms

MCRT	Monte Carlo Ray-Tracing
RMS	Root Mean Square deviation
SPT	Solar Power Tower

model, which will ultimately increase the reliability of SPT design and operation tools.

The manuscript is structured as follows. In Section 2, the theoretical background is presented for both UNIZAR analytic function and heliostat astigmatism. In Section 3, after a geometric characterization of astigmatism and defocus, the reflection of heliostat axes is analyzed. From previous insights, Section 4 presents an analytic function that accounts for defocus and astigmatism. Finally, the resulting model is contrasted with MCRT, and the model validity is assessed in Section 5.

2. Theoretical background

Firstly, UNIZAR analytic function is introduced, followed by the mathematical background behind astigmatic phenomena.

2.1. UNIZAR analytic function

Collado et al. (1986) developed an analytic model for the solar flux distribution produced by focused heliostats. Specifically, two analytic functions, named UNIZAR (Collado, 2010), were proposed: one at the image plane (i.e., plane perpendicular to the main reflected ray) and another at the receiver plane. Because of the conformal mapping property (preservation of angles) existing between heliostat and image plane, its analytic function is herein utilized as the starting point. Whether the flux distribution is required at the receiver surface, a projection method can be utilized, as described elsewhere (Sánchez-González and Santana, 2015).

The flux density distribution F on the image plane follows Eq. (1) according to UNIZAR analytic function. This function results from the convolution of concentration, sunshape and optical errors, that are modeled as circular Gaussians. Therefore, UNIZAR function represents a two-dimensional Gaussian distribution that is evaluated at ξ and ζ, heliostat coordinates on the image plane. The $\mathcal{H}$ function, defined in Eq. (2), is precisely a combination of the Gaussian error function, erf (Eq. (3)).

$$F(\xi,\zeta)=\frac{\cos\omega}{J}\eta_{ref}\eta_{sb}\eta_{at}I_d\frac{A_m}{A_h}\mathcal{H}(\xi,-aw,aw)\mathcal{H}(\zeta,-ah,ah) \tag{1}$$

$$\mathcal{H}(x,a,c)=0.5\cdot[erf\,(x-a)-erf\,(x-c)] \tag{2}$$

$$erf(x)=\frac{2}{\sqrt{\pi}}\int_0^x e^{-t}dt \tag{3}$$

UNIZAR analytic function (Eq. (1)) comprises the direct normal irradiation (I_d), the ratio of mirror to heliostat areas (A_m/A_h), and the optical loss factors – except spillage –, namely: cosine ($\cos\omega$),

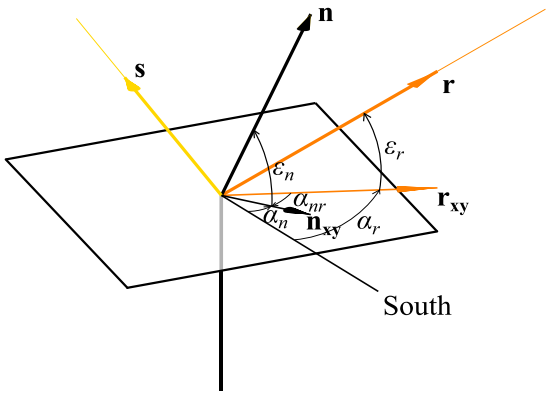

Fig. 1. Azimuth and elevation angles of heliostat normal (**n**) and reflected vector (**r**).

reflectivity (η_{ref}), shading and blocking (η_{sb}), and attenuation (η_{at}). Along with the previous parameters, Eq. (1) comprises the Jacobian of the conformal mapping (J). This Jacobian results from the transformation matrix from image to heliostat coordinate systems and follows Eq. (4). Further details on UNIZAR function can be found in Collado et al. (1986). Since another formulation of the Jacobian will be later presented, subscript uz is specific to the original UNIZAR analytic function on the image plane.

$$J_{uz} = (1 - \cos\omega)^2 \tag{4}$$

UNIZAR function assumes spherical, continuous, focused and on-axis aligned heliostats (Collado et al., 1986). Given a single mirror of curvature radius R, its focal length is $f = R/2$. Defining D slant range as the mirror-to-target distance, the focused assumption is equivalent to: $D = f$.

Under these circumstances, the reflection of curved mirrors onto the image plane –also named heliostat image– follows conformal mapping. Such a mapping entails a scaling and a rotation of the heliostat image. The scaling is included through the Jacobian J, previously defined in Eq. (4), and the Gaussian effective error σ_e. This effective error results from the convolution of sunshape (σ_{sun}), mirror slope error (σ_{slp}), and heliostat tracking error (σ_{trk}); as declared in Eq. (5).

$$\sigma_e = \sqrt{\sigma_{sun}^2 + 2\left(1 + \cos^2\omega\right)\sigma_{slp}^2 + \sigma_{trk}^2} \tag{5}$$

On the other hand, the rotation of the heliostat image with respect to the image plane system of coordinates is defined by θ rotation angle. For focused heliostats, Collado et al. (1986) determined the rotation angle (θ_{uz}) as a function of azimuth (α) and elevation (ϵ) angles of the heliostat normal (**n**) and the reflected vector (**r**), shown in Fig. 1. The mathematical expression is in Eq. (6), where $\alpha_{nr} = \alpha_n - \alpha_r$.

$$\theta_{uz} = \arctan\left(\frac{-\cos\epsilon_r \sin\alpha_{nr} + \cos\epsilon_n \sin\alpha_{nr}}{-\cos\alpha_{nr} + \cos\epsilon_n \cos\epsilon_r \cos\alpha_{nr} + \sin\epsilon_n \sin\epsilon_r}\right) \tag{6}$$

The system of coordinates of the image plane (x_{si} and y_{si}) is orthogonal, similarly to the system of coordinates of the heliostat image (ξ and ζ, in Eq. (1)). Both systems are linearly related and can be transformed from one to the other. This transformation, expressed in Eq. (7), entails the aforementioned scaling and rotation of the heliostat image, therefore depending on σ_e and θ_{uz}.

$$\begin{aligned}\xi_{uz} &= \frac{x_{si}\cos\theta_{uz} + y_{si}\sin\theta_{uz}}{\sqrt{2}\cdot D\cdot\sigma_e}\\ \zeta_{uz} &= \frac{y_{si}\cos\theta_{uz} - x_{si}\sin\theta_{uz}}{\sqrt{2}\cdot D\cdot\sigma_e}\end{aligned} \tag{7}$$

Given a rectangular heliostat of LW width and LH height, its reflection on the image plane has lw and lh dimensions. Because of conformal mapping, the original dimensions are affected by the square root of the Jacobian, as expressed in Eq. (8). This expression is valid for focused heliostats ($f = D$), therefore subscript uz is again utilized in Eq. (8). The integration limits, aw and ah in Eq. (1), result from the scaling of lw and lh to the ξ and ζ system of coordinates, as computed with Eq. (9).

$$\begin{aligned}lw_{uz} &= LW\sqrt{J_{uz}}\\ lh_{uz} &= LH\sqrt{J_{uz}}\end{aligned} \tag{8}$$

$$\begin{aligned}aw &= \frac{lw/2}{\sqrt{2}\cdot D\cdot\sigma_e}\\ ah &= \frac{lh/2}{\sqrt{2}\cdot D\cdot\sigma_e}\end{aligned} \tag{9}$$

To make it independent of the instantaneous direct normal irradiation (I_d), the analytic function can be expressed in terms of C concentration ratio of flux density ($C = F/I_d$). In an ideal case where the optical loss factors (η_{ref}, η_{sb}, η_{at}) –except the cosine factor that is inherent to solar position– are equal to 1, as well as A_m/A_h, Eq. (1) turns into the Eq. (10). As long as the two-dimensional coordinates ξ_{uz} and ζ_{uz} are related to x_{si} and y_{si} coordinates on the image plane (Eq. (7)), the concentration ratio is expressed as $C_{uz}(x_{si}, y_{si})$. The structure of this expression of the concentration ratio of flux density on the image plane, which is specific for ideal heliostats (UNIZAR), will be taken as reference for the analytic function later proposed in Section 4.

$$\begin{aligned}C_{uz}(x_{si}, y_{si}) = \frac{\cos\omega}{J_{uz}}\cdot 0.25\cdot &\left[erf\left(\xi_{uz} + aw\right) - erf\left(\xi_{uz} - aw\right)\right]\\ \cdot &\left[erf\left(\zeta_{uz} + ah\right) - erf\left(\zeta_{uz} - ah\right)\right]\end{aligned} \tag{10}$$

2.2. Astigmatism

In on-axis incidence –sun pointing vector coincides with heliostat normal vector– the reflected beams collide in a single focus at a distance $f = R/2$ from the spherical heliostat of R radius. The sun, heliostat and target centers must be aligned to be on-axis, which is a singularity in SPT systems and actually leads to heliostat shading by the target. Therefore, off-axis incidence is the general rule with angles of incidence on the heliostat different to zero ($\omega \neq 0$).

Astigmatic aberrations appear on the flux distribution for off-axis incidence. Instead of a single focus, two foci emerge from the bundle of reflected rays. These foci are named tangential and sagittal focus, with f_t and f_s focal lengths. From classical optics (Coddington, 1825), the tangential and sagittal focal lengths are respectively determined by Eqs. (11) and (12), which depend on the cosine of the incidence angle.

$$f_t = f\cos\omega \tag{11}$$

$$f_s = \frac{f}{\cos\omega} \tag{12}$$

The tangential plane is that containing the heliostat normal and the main sunray, defined as the ray from the sun center to the heliostat center. The sagittal plane is perpendicular to the tangential plane. Both planes contain the main reflected ray, defined as the ray from the heliostat center to the target point. For a heliostat of L characteristic length –i.e. circular reflector–, Fig. 2 shows two views: the tangential plane (top) and the sagittal plane (bottom). As dictated by the previous Equations, the tangential focus at f_t takes place nearer to the reflector than the sagittal focus at f_s. The flux distribution at the nominal focus (f) is known as circle of least confusion, at which UNIZAR analytic function is precisely valid ($D = f$).

Fig. 2 identifies the length of the reflected heliostat image in tangential (l_t) and sagittal (l_s) directions, which depend on the specific D slant range. Igel and Hughes (1979) and Biggs and Vittitoe (1979) stated the geometric relationships in the tangential (Eq. (13)) and sagittal

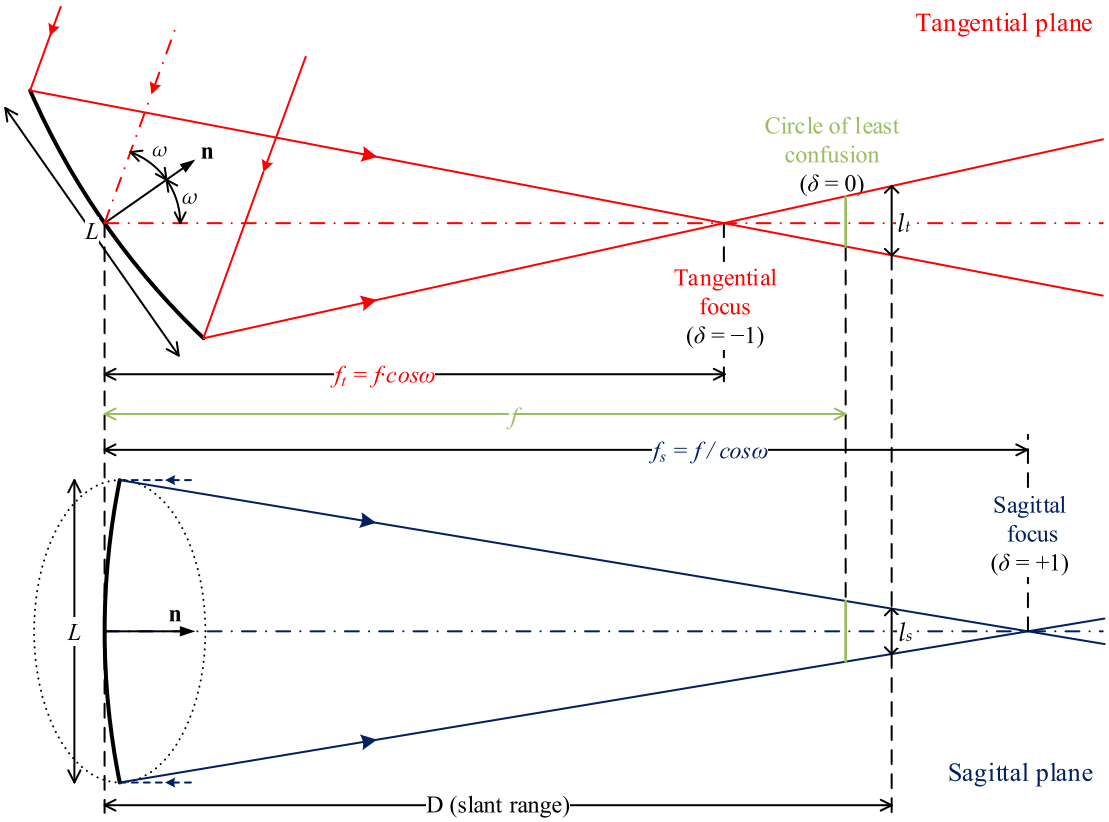

Fig. 2. Tangential (top) and sagittal (bottom) ray fans for circular reflector of f nominal focal length.

(Eq. (14)) planes. The size of the sun is neglected herein as long as it is accounted for within σ_e effective error.

$$\frac{L\cos\omega}{f_t} = \frac{l_t}{D - f_t} \tag{13}$$

$$\frac{L}{f_s} = \frac{l_s}{f_s - D} \tag{14}$$

From previous Equations, Igel and Hughes (1979) and Biggs and Vittitoe (1979) solved the reflected lengths in tangential (Eq. (15)) and sagittal (Eq. (16)) directions. These expressions provide a straight measurement of the astigmatic aberrations depending on ω incidence angle and D slant range, that differs from f nominal focal length under defocus. From equivalent expressions, Hénault (2015) obtained representations of astigmatism in circular heliostats as a function of ω and defocus $(D - f)$.

$$l_t = L\left|\frac{D}{f} - \cos\omega\right| \tag{15}$$

$$l_s = L\left|1 - \frac{D}{f}\cos\omega\right| \tag{16}$$

3. Analysis on defocus: axes reflection

This Section characterizes the relevant optics for heliostats under defocus. Firstly, the geometrical parameters are defined. Later, the reflection of heliostat axes is analyzed.

3.1. Geometric characterization

Image planes are those normal to the main reflected ray (**r**) at any D distance from the mirror. If the distance is the mirror focal length, the flux distribution is named circle of least confusion; otherwise, the flux distribution is affected by defocus. Image planes are herein utilized to generate the flux maps by single mirrors. Relevant angles and dimensions are defined for a proper interpretation.

Fig. 3(a) shows a 3D representation of the image plane, along with tangential and sagittal planes. The Figure specifies the coordinate systems of image plane (si), heliostat (sh), and global (sg). As previously described, the tangential plane contains **r** and the heliostat normal **n**, as well as **s** sun pointing vector at the heliostat center. The sagittal plane is perpendicular to the tangential plane and contains **r** vector. As long as the image plane is perpendicular to **r**, image, tangential and sagittal planes are perpendicular to each other.

The intersection of tangential and sagittal planes with the image plane is respectively named tangential and sagittal axis, as depicted in Fig. 3(a). At any image plane, tangential and sagittal axes keep fixed and perpendicular, since these three planes are orthogonal. The angle between the tangential axis and the vertical axis of the image plane (Y_{si}) is defined as β angle. Because of the orthogonality property, the same β angle exists between the sagittal axis and the horizontal axis of the image plane (X_{si}).

Fig. 4 shows, for two different slant ranges, 2D views of the image plane with the representation of tangential and sagittal axes. Throughout the paper, a dashed black line is utilized for the tangential axis, and a solid black line for the sagittal axis. Regardless of D slant range, β angle is unique and constant given a heliostat and sun position. Taking advantage of vector notation, β angle can be calculated as the angle between Y_{si} and the projection of **s** sun vector onto the image plane. For the transformation of coordinates systems, the reader is referred to Sánchez-González and Santana (2015).

To analyze the effect of defocus on the flux distribution, we are interested in characterizing the reflection of the heliostat, or its axes, into the image planes. As shown in Fig. 3(b), the horizontal and vertical axes of a rectangular heliostat (LW width and LH height) can be reflected into any image plane. The color coding shown in the Figure will be utilized throughout the whole manuscript: horizontal axis in blue, and vertical axis in green.

Applying Snell's law on the heliostat axes, their reflection into image planes can be computed by means of vector operations. Two angles

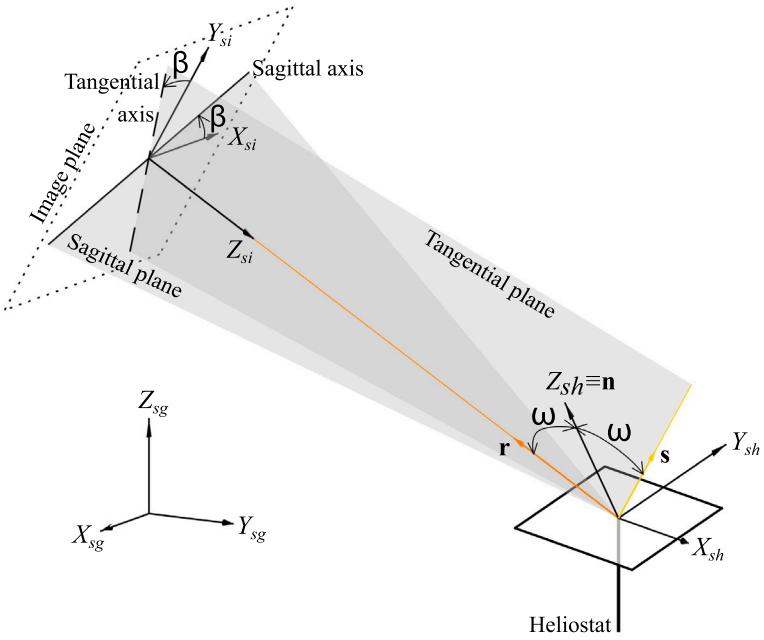

(a) Tangential and sagittal planes. Heliostat, image and global coordinate systems. β and ω angles.

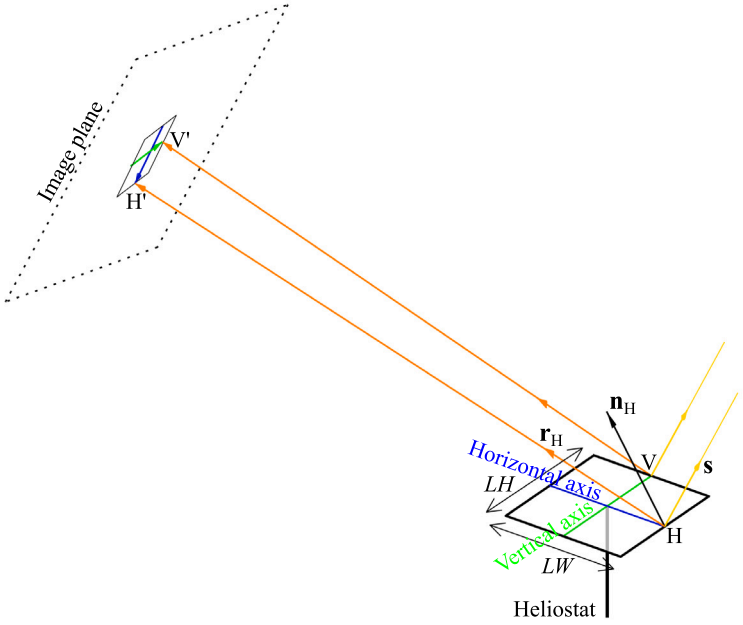

(b) Reflection of heliostat axes on image plane.

Fig. 3. 3D views for geometric characterization.

with respect to the horizontal axis of the image plane are identified. θ_H is the angle between the reflection of the heliostat horizontal axis (blue) and X_{si}. Similarly, θ_V is the angle between the reflection of the heliostat vertical axis (green) and X_{si}. These two angles are labeled in the two representations of image planes in Fig. 4. Both θ_H and θ_V are considered positive in counterclockwise direction, as depicted in Appendix provides the vector procedure to obtain θ_H and θ_V angles.

Unlike the β angle which is invariant with the slant range, the reflections of the heliostat axes evolve depending on the distance to the image plane. For focused heliostats (image plane at $D = f$), the reflected axes are orthogonal as represented in Fig. 4(a). Then $\theta_V = \theta_H + 90°$ and θ_H is equal to UNIZAR θ_{uz} angle (Eq. (6)). However, for defocused heliostats (image plane at $D \neq f$), the reflected axes are not perpendicular, therefore $\theta_V \neq \theta_H + 90°$ and θ_H is different to θ_{uz} (Fig. 4(b)). The evolution of θ_H and θ_V depending on defocus is analyzed at the end of this Section.

Another angle that will have a key role later on is that between the sagittal axis and the heliostat horizontal axis when focused. Namely, $\Delta\theta_s$ is the difference between β and θ_{uz}, as expressed in Eq. (17) and graphically depicted in Fig. 4(a). This difference angle, $\Delta\theta_s$, defines the dominant direction: sagittal if $< 45°$, or tangential if $\geq 45°$. As $\Delta\theta_s$ is defined between 0° and 90°, if the result from the Eq. (17) is greater than 90°, then it must be recomputed as $\Delta\theta_s = 180° - \Delta\theta_s$.

$$\Delta\theta_s = |\beta - \theta_{uz}| \tag{17}$$

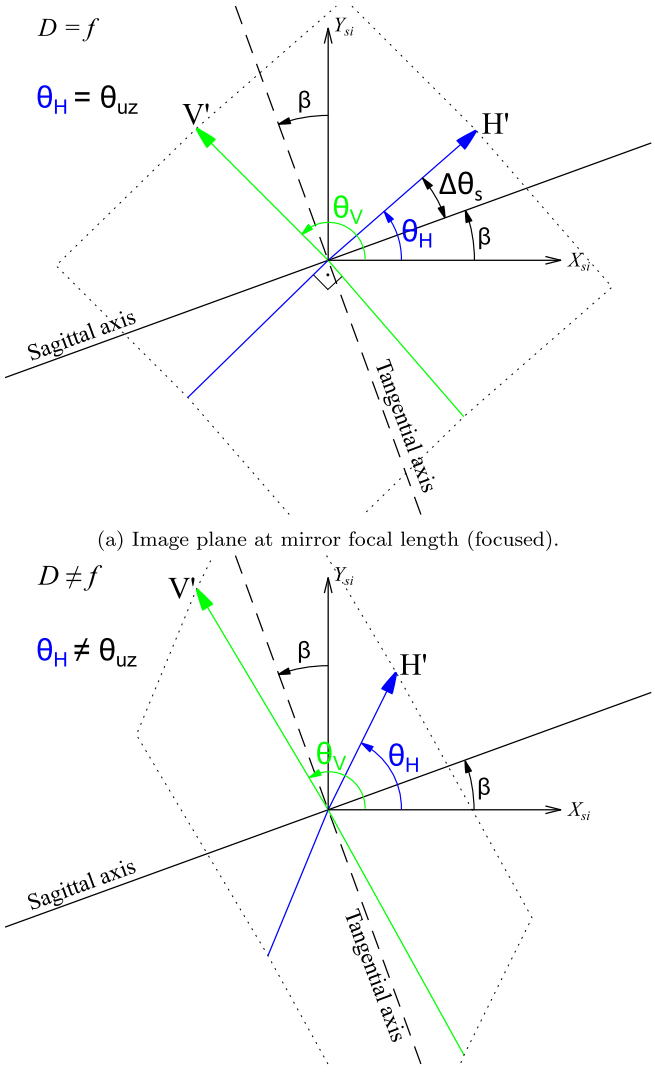

(a) Image plane at mirror focal length (focused).

(b) Image plane not at mirror focal length (defocused).

Fig. 4. Image planes, at two slant ranges, showing: tangential and sagittal axes (β angle), and reflection of heliostat horizontal and vertical axes (θ_H and θ_V angles).

3.2. Non-dimensional parameters

To analyze the effect of defocus, several parallel image planes at different D distances from the reflector will be considered. These image planes virtually range between the tangential focus at f_t and the sagittal focus at f_s. To identify these planes, it is defined δ as the relative distance to the circle of least confusion. This dimensionless parameter is calculated with Eq. (18).

$$\delta = \frac{D - f}{|f^* - f|} \quad \text{, where } f^* = \begin{cases} f_t = f\cos\omega & \text{, if } D < f \\ f_s = f/\cos\omega & \text{, if } D > f \end{cases} \tag{18}$$

Thus, δ ranges between -1 at the tangential focus ($D = f_t$), and $+1$ at the sagittal focus ($D = f_s$), being 0 at the mirror focal length ($D = f$). The δ relative distance to the circle of least confusion was already displayed in Fig. 2

Because of the optical scaling properties of central receiver systems (Winter et al., 1991), except for the atmospheric attenuation depending on the specific D slant range, dimensions can be expressed as non-dimensional parameters with respect to the mirror length. Herein the heliostat height (LH) is taken as the reference dimension. Consequently, the non-dimensional heliostat width is $L\hat{W} = LW/LH$, the non-dimensional focal length is $\hat{f} = f/LH$, and the non-dimensional slant range is $\hat{D} = D/LH$; the hat over the symbol denotes non-dimensional lengths. This means that for $LH = 1$ m, the remaining lengths are in meters too. Results in this paper will be presented in terms of non-dimensional lengths, this way taking advantage of the scaling property of point focus systems.

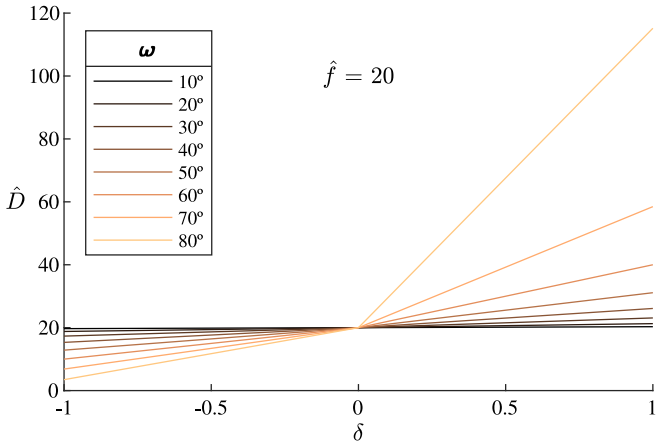

Fig. 5. For $\hat{f} = 20$, non-dimensional slant range $\hat{D}$ as a function of incidence angle (ω) and relative distance to the circle of least confusion (δ).

From Eq. (18), the non-dimensional slant range ($\hat{D}$) can be represented as a function of the relative distance to the circle of least confusion (δ), as well as $\hat{f}$ and ω. For non-dimensional focal length equal to 20, Fig. 5 shows the resulting $\hat{D}$. For instance, for $\omega = 60°$, the tangential focus is at $\hat{D} = 10$ and the sagittal focus is at $\hat{D} = 40$. From the Figure, it is clear that $\hat{D}$ is linearly dependent on δ with two intervals with different slope: before ($\delta < 0$) and after ($\delta > 0$) the mirror focal length.

3.3. Reflection of heliostat axes

Under defocus and astigmatism, the flux distributions on the image planes take spot shapes similar to the reflection of the heliostat. Therefore, we are interested in analyzing how does the reflection of heliostat axes evolves depending on the slant range. Given a heliostat with fixed $\hat{f}$ focal length, its axes are reflected into parallel image planes between the tangential focus ($\delta = -1$) and the sagittal focus ($\delta = 1$).

For a rectangular reflector of width twice its height ($LW = 2 \cdot LH$) and $\hat{f} = 20$, Fig. 6 shows the reflection of its axes when the incidence angle is 60°. At the circle of least confusion ($\delta = 0$), the reflected horizontal (blue) and vertical (green) axes are perpendicular, as assumed by UNIZAR. Indeed, θ_H equals θ_{uz} at the focal length. As the difference angle between θ_{uz} and β (Eq. (17)), named $\Delta\theta_s$, is greater than 45°, the tangential direction is dominant for this heliostat configuration.

At all the image planes, Fig. 6 displays the angles between the reflected axes and the image horizontal axis (X_{si}). These θ_H and θ_V angles, that will play a relevant role in the proposed analytic function, are computed as described in Appendix. The arrowheads signal the positive endpoints of the reflected axes, i.e. H' and V' like in conceptual Figs. 3(b) and 4.

As can be seen in Fig. 6, the reflected axes line up along the sagittal axis at the tangential focus ($\delta = -1$). Conversely, the reflected axes line up along the tangential axis at the sagittal focus ($\delta = 1$). This is in agreement with the astigmatism background described in Section 2.2, graphically summarized in Fig. 2.

Having a look at the evolution of the reflected axes from the tangential to the sagittal focus (Fig. 6), the horizontal axis (blue) rotates counterclockwise and the vertical axis (green), clockwise. Similarly, the length of the reflected axes increases with the slant range.

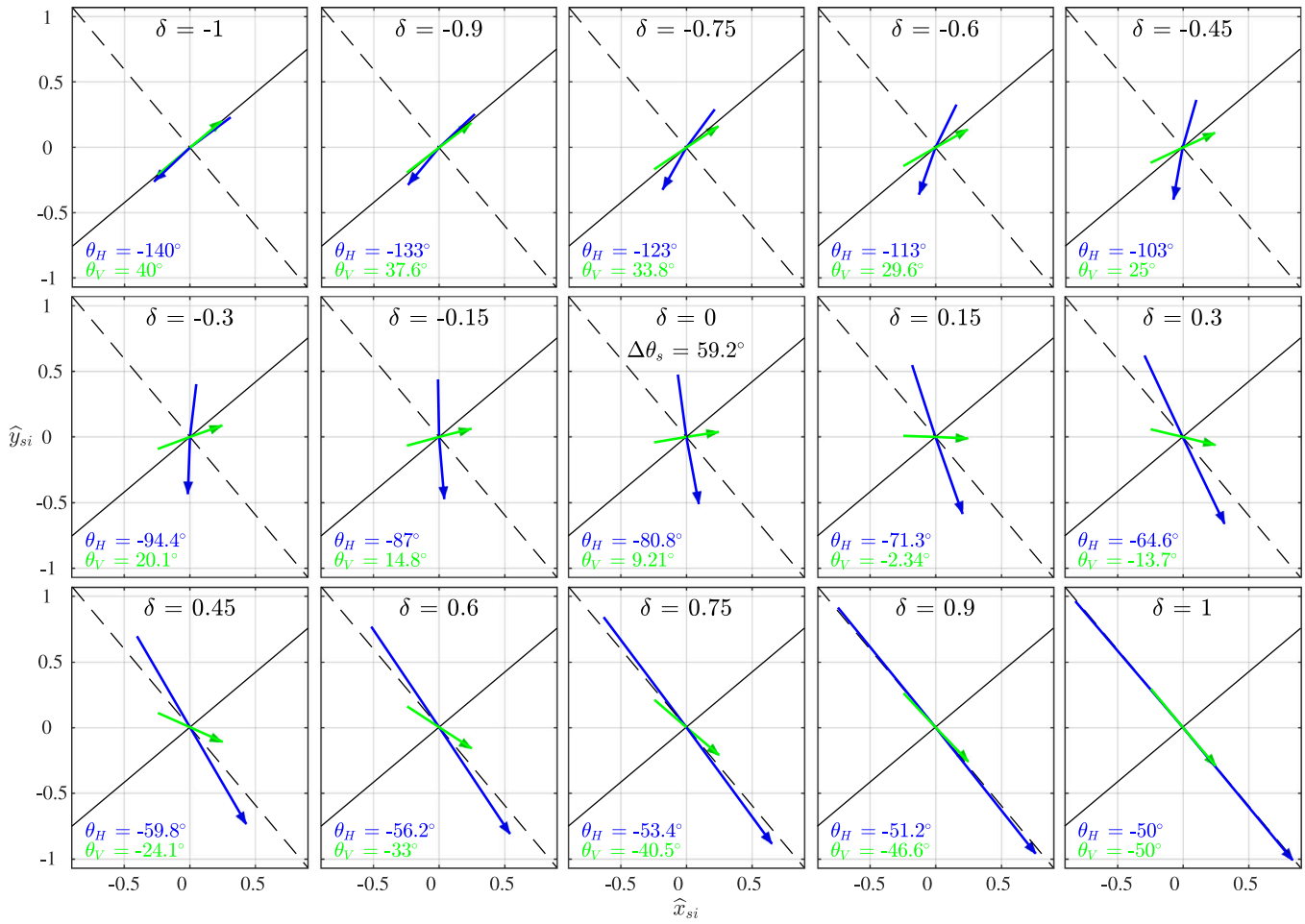

Fig. 6. Reflection of horizontal (blue) and vertical (green) axes of a rectangular heliostat ($L\hat{W} = 2$) of $\hat{f} = 20$. Angles: $\omega = 60°$, $\beta = 40°$.

4. Analytic function with defocus and astigmatism

Section 2 stated the background on UNIZAR function and astigmatism principles. The reflected lengths of the heliostat in tangential and sagittal directions result from Eqs. (15) and (16). For focused heliostats, both reflected lengths are the same (circular reflector), turning into Eq. (19). In UNIZAR model for rectangular heliostats, the lengths of reflection were established by Eq. (8). Making the analogy between such Eqs. (8) and (19), it is clear that the term in absolute value in the latter Equation is the square root of UNIZAR Jacobian (Eq. (4)).

$$l_t = l_s = L|1 - \cos\omega| \equiv L\sqrt{J_{uz}} \qquad (\text{if } D = f) \tag{19}$$

For defocused heliostats, the same analogy applies. Thus, the terms in absolute value in Eqs. (15) and (16) can be identified as the Jacobians in tangential (J_t) and sagittal (J_s) directions, as stated in Eqs. (20) and (21). Instead of the unique Jacobian (J_{uz}) utilized by UNIZAR, these two Jacobians are required to characterize mirrors with defocus. From their definition, J_t becomes zero at the tangential focus ($D = f\cos\omega$) and $J_s = 0$ at the sagittal focus ($D = f/\cos\omega$).

$$J_t = \left(\frac{D}{f} - \cos\omega\right)^2 \tag{20}$$

$$J_s = \left(1 - \frac{D}{f}\cos\omega\right)^2 \tag{21}$$

Following the structure of UNIZAR Eq. (8), the reflected lengths by rectangular defocused heliostats will be affected by the tangential and sagittal Jacobians. The reflected length depends on the dominant direction. If the sagittal direction is dominant ($\Delta\theta_s < 45°$), then $lw = LW\sqrt{J_s}$ and $lh = LH\sqrt{J_t}$, otherwise the Jacobians swap. Eqs. (22) and (23) state the piecewise relations for the reflected width and height, respectively. At the tangential ($J_t = 0$) and the sagittal ($J_s = 0$) focus, one of the reflected lengths becomes zero, which is in agreement with the analysis in previous Sections.

$$lw = \begin{cases} LW\sqrt{J_s} & , \text{if } \Delta\theta_s < 45° \\ LW\sqrt{J_t} & , \text{if } \Delta\theta_s \geq 45° \end{cases} \tag{22}$$

$$lh = \begin{cases} LH\sqrt{J_t} & , \text{if } \Delta\theta_s < 45° \\ LH\sqrt{J_s} & , \text{if } \Delta\theta_s \geq 45° \end{cases} \tag{23}$$

Under defocus, the reflected heliostat axes are non-orthogonal. The two directions are set by θ_H and θ_V angles. The transformation of x_{si} and y_{si} coordinates into ξ' and ζ' (the prime denotes non-orthogonal directions) depends on both angles. This transformation follows Eq. (24). The procedure to determine these two rotation angles (θ_H and θ_V) can be found in Appendix.

$$\begin{aligned} \xi' &= \frac{y_{si}\cos\theta_V - x_{si}\sin\theta_V}{\sqrt{2}\cdot D\cdot\sigma_e} \\ \zeta' &= \frac{y_{si}\cos\theta_H - x_{si}\sin\theta_H}{\sqrt{2}\cdot D\cdot\sigma_e} \end{aligned} \tag{24}$$

While UNIZAR function (Eq. (10)) assumes conformal mapping, it is required a proper transformation from non-orthogonal $\xi' - \zeta'$ to orthogonal $\xi - \zeta$ coordinate systems. Keeping fixed one of the directions (primary), the projection of the other direction (secondary) to the normal of the primary one must be undone. Mathematically, this is achieved by dividing by the sine of the angle between the heliostat

reflected horizontal and vertical axes: $|\sin(\theta_H - \theta_V)|$. Depending on the dominant direction ($\Delta\theta_s$) and the defocus region ($\delta < 0$ or $\delta > 0$), the ultimate ξ and ζ coordinates respectively result from piecewise Eqs. (25) and (26).

$$\xi = \begin{cases} \dfrac{\xi'}{|\sin(\theta_H - \theta_V)|} & \begin{cases} \text{if} \quad \Delta\theta_s < 45° \quad \& \quad D < f \text{ , or} \\ \text{if} \quad \Delta\theta_s \geq 45° \quad \& \quad D > f \end{cases} \\ \xi' & \text{otherwise} \end{cases} \tag{25}$$

$$\zeta = \begin{cases} \dfrac{\zeta'}{|\sin(\theta_H - \theta_V)|} & \begin{cases} \text{if} \quad \Delta\theta_s < 45° \quad \& \quad D > f \text{ , or} \\ \text{if} \quad \Delta\theta_s \geq 45° \quad \& \quad D < f \end{cases} \\ \zeta' & \text{otherwise} \end{cases} \tag{26}$$

The analytic function of flux concentration on the image plane for rectangular heliostats under defocus follows the same structure as UNIZAR function (Eq. (10)). Now, instead of ξ_{uz} and ζ_{uz} coordinates, ξ (Eq. (25)) and ζ (Eq. (26)) applies, so that the analytic function turns into Eq. (27). The limits of integration (aw and ah) still result from Eq. (9), but lw and lh must be calculated with previous Eqs. (22) and (23). If reflectivity, shading and blocking, and attenuation losses are considered, the corresponding factors (η_{ref}, η_{sb} and η_{at}) must be included in Eq. (27).

$$C(x_{si}, y_{si}) = \frac{\cos\omega}{J} \cdot 0.25 \cdot [erf(\xi + aw) - erf(\xi - aw)] \cdot [erf(\zeta + ah) - erf(\zeta - ah)] \tag{27}$$

The Jacobian, J, now is not a single one, but a couple of them: J_t (Eq. (20)) and J_s (Eq. (21)). To comply with the conservation of incident energy on the image plane, the Jacobian must be the geometric mean of J_t and J_s, as expressed in the following Equation.

$$J = \sqrt{J_t J_s} \tag{28}$$

This analytic function for heliostats with defocus (Eq. (27)), however, is indeterminate at the tangential and sagittal foci. There, one of the Jacobians becomes zero, and ξ and ζ are indeterminate as $|\sin(\theta_H - \theta_V)| = 0$. Therefore, the application of the proposed analytic function is valid from the tangential up to the sagittal focal planes, excluding both of them.

It is important to note that for focused reflectors, the proposed analytic function is equivalent to UNIZAR. This is true as long as, for $D = f$, the Jacobians ($J_t = J_s = J_{uz}$) and the rotation angles ($\theta_H = \theta_{uz}$) become the same. Similarly to UNIZAR, the proposed analytic function is valid for rectangular mirrors, either a whole heliostat or its mirror facets.

5. Results: verification

This Section verifies the presented analytic function for single defocused heliostats. Monte Carlo Ray-Tracing simulations are contrasted against the proposed model. SolTrace, MCRT freeware developed by NREL (Wendelin et al., 2013), is utilized for the verification. Concentration maps are compared in the next Subsection, followed by an analysis of the validity of the model.

5.1. Flux maps

Flux distributions by the model are compared with those by SolTrace, to assess the ability of the proposed model to reproduce astigmatic phenomena by single heliostats under defocus. As obtained from the analytic function (Eq. (27)), flux maps are expressed in terms of C concentration ratio of flux density, which is independent of the instantaneous direct normal irradiation.

To assess the coincidence of the model with respect to MCRT, the cross-correlation coefficient (ρ) is used as figure of merit. From C concentration ratio by the model (mod) and SolTrace (st) at each n point in the image plane, the cross-correlation coefficient is calculated with Eq. (29), where $\overline{C}$ and $\sigma(C)$ respectively stand for the average and the standard deviation of C in the whole meshgrid consisting of N points. Along with ρ, the root mean square deviation (RMS) of the concentration ratio is provided in the comparison between flux maps.

$$\rho = \frac{1}{N-1} \sum_{n=1}^{N} \left(\frac{C_{st,n} - \overline{C_{st}}}{\sigma(C_{st})} \right) \left(\frac{C_{mod,n} - \overline{C_{mod}}}{\sigma(C_{mod})} \right) \tag{29}$$

Given a reflector with f focal length, the flux maps are generated at image planes both before and after the circle of least confusion. Specifically, this Section shows results in the range from $\delta = -0.8$ to $\delta = 0.8$, in steps of 0.2. Since the analytic function is indeterminate at the tangential ($\delta = -1$) and sagittal ($\delta = 1$) focus, both image planes are discarded.

A large number of cases were run both in SolTrace and the model. For SolTrace simulations, 20 million rays were traced in each case. Because of the effect of actual sunshape and incidence angles on the flux distribution (Landman et al., 2016), a Kuiper sunshape model (Biggs and Vittitoe, 1979) is introduced in SolTrace simulations. As deduced by Schwarzbözl et al. (2009), Kuiper sunshape is statistically comparable to a Gaussian distribution of $\sigma_{sun} = 2.24$ mrad which has been considered for the proposed and UNIZAR models. In all the cases, a moderate mirror slope error of $\sigma_{slp} = 1$ mrad and no tracking error ($\sigma_{trk} = 0$) have been considered.

In order to compare the spatial flux distributions by single mirrors, reflectivity and atmospheric attenuation losses are disregarded as long as they do not affect the flux shape and produce the same absolute effect (same flux reduction) both in MCRT and analytic models. Whether specific dimensions are considered, a proper correlation for the atmospheric attenuation must be utilized (Hanrieder et al., 2017). Taking advantage of the scaling property of SPT systems, lengths are expressed in terms of non-dimensional parameters. For illustration purposes, three configurations are shown in this Subsection.

The first case, in Fig. 7, corresponds to a square heliostat ($L\hat{W} = 1$) of non-dimensional focal length $\hat{f} = 20$. To reproduce astigmatic phenomena, a large incidence angle of $\omega = 60°$ is considered. β angle is 40°. For this case, Fig. 7 shows nine concentration maps, where the contour isolines are solid and dotted respectively for the model and SolTrace. For proper comparison, the concentration levels of the six isolines are fixed at each image plane, according to the values in each colorbar.

Starting from the image plane at the focal length ($\delta = 0$), the modeled concentration map (central one in Fig. 7) is almost the same as that predicted by UNIZAR. The heliostat image shows a quasi-square shape with rounded corners that virtually matches the MCRT simulation ($\rho = 0.992$). At image planes towards the tangential focus, the spot takes a quasi-rhomboid shape that lines up along the sagittal axis while δ decreases. Contrarily, while δ increases (image planes towards the sagittal focus), quasi-rhomboid distributions line up along the tangential axis. The size of the spot increases with slant range, while the concentration levels consequently decrease.

The model reproduces similar distributions to MCRT, even though the cross-correlation coefficient slightly decreases while approaching the astigmatic foci. The lowest correlation (85.2%) takes place near to the sagittal focus ($\delta = 0.8$). While the analytic function leads to a very stretched rhomboid-like shape, the MCRT map tends towards an elliptical pattern.

In a second configuration, the heliostat is rectangular, the width being twice the height ($L\hat{W} = 2$), and with the same focal length ($\hat{f} = 20$). Fig. 8 shows the concentration maps for 50° of incidence angle and 20° of β angle. The heliostat shape (rectangular of $LW = 2 \cdot LH$) with rounded corners is again noticeable in the circle of least confusion ($\delta = 0$). As $\Delta\theta_s$ is smaller than 45°, the sagittal direction is dominant in this case.

Good agreement between the model and SolTrace is shown in Fig. 8. Although the correlation coefficient decreases when approaching the astigmatic foci, coefficients are greater than 90% at $\delta = \pm 0.8$. At these slant ranges, the isolines of high C (red) fit fairly well to SolTrace.

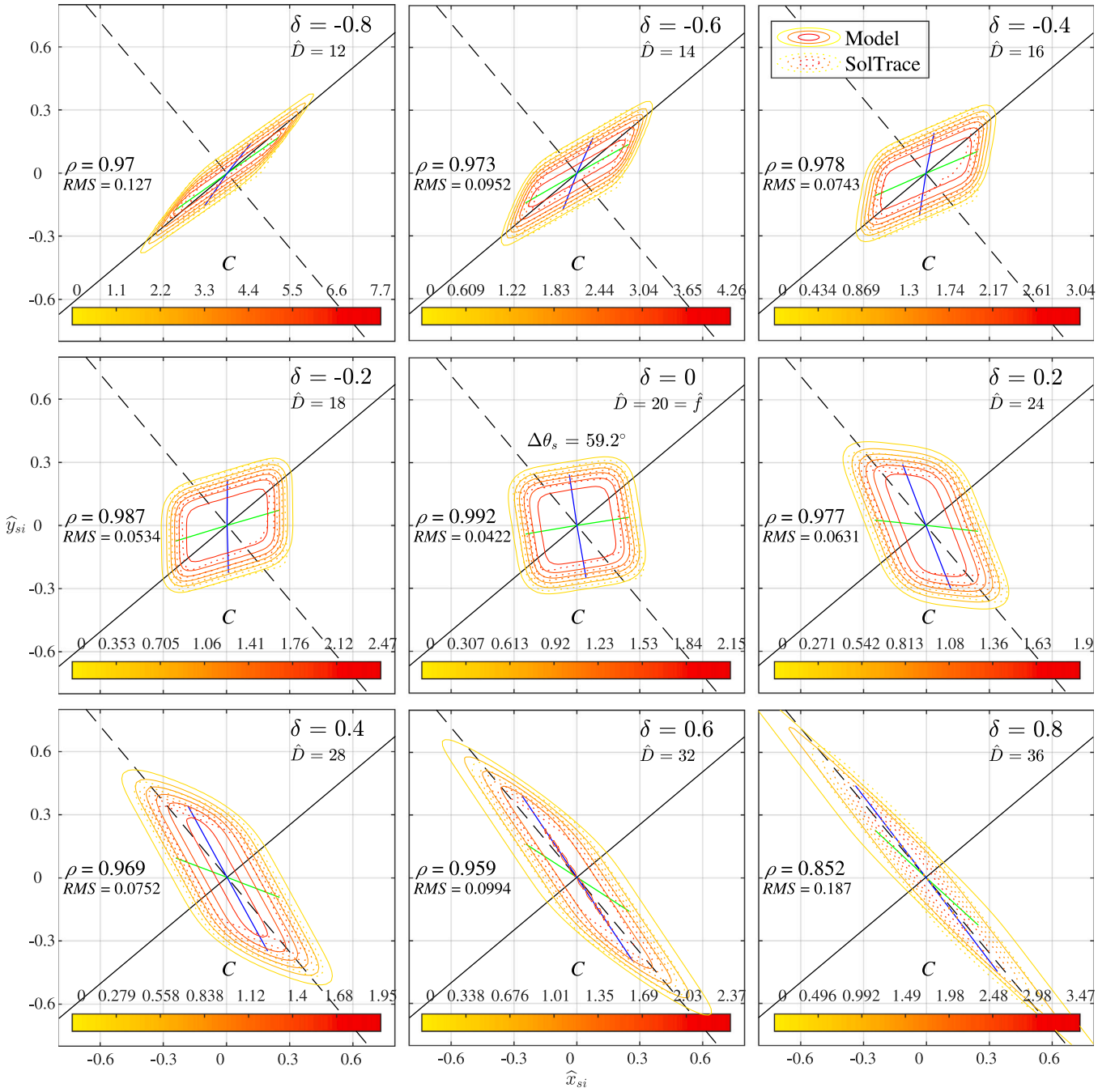

Fig. 7. Concentration maps in the image plane by the model (solid isolines) and SolTrace (dotted) for several δ relative distances. Angles: $\omega = 60°$, $\beta = 40°$. Mirror: $\hat{f} = 20$, $LW = LH$. (For interpretation of the references to color in this figure legend, the reader is referred to the web version of this article.)

In a third configuration (Fig. 9), the rectangular heliostat ($L\hat{W} = 2$) has a non-dimensional focal length of $\hat{f} = 50$ and $\beta = 60°$. For an incidence angle of 30°, Fig. 9(a) shows the concentration maps. SolTrace simulates elliptical spots that rotate counterclockwise while the slant range increases. The model predicts such rotations, together with an additional stretching that is greater than expected. Such elongations are particularly excessive near the astigmatic foci, where the correlation coefficient drops to around 60%.

For the same configuration, but a larger incidence angle of 60°, Fig. 9(b) shows the flux maps. A better fitting between the model and SolTrace is now achieved, with correlation coefficients above 90%, except when reaching the sagittal focus where the correlation drops to 78.4% ($\delta = 0.8$). Consequently, the proposed model reproduces more accurately the distributions produced by defocused heliostats with high incidence angles, that is, when the astigmatic aberrations are noteworthy.

5.2. Model validity

In the previous Subsection, just a few cases were shown. To check the validity of the model, the cross-correlation coefficient is analyzed in a long series of cases. Both the correlation coefficients by the proposed model and UNIZAR, with respect to SolTrace simulations, are provided in the following.

For $\hat{f} = 20$, Fig. 10 summarizes the correlation coefficients with incidence angles from 10° to 80°, in steps of 10°. The relative distance to the circle of least confusion, δ, is accounted for in the horizontal axis of each graph. Each color family denotes a β angle, according to

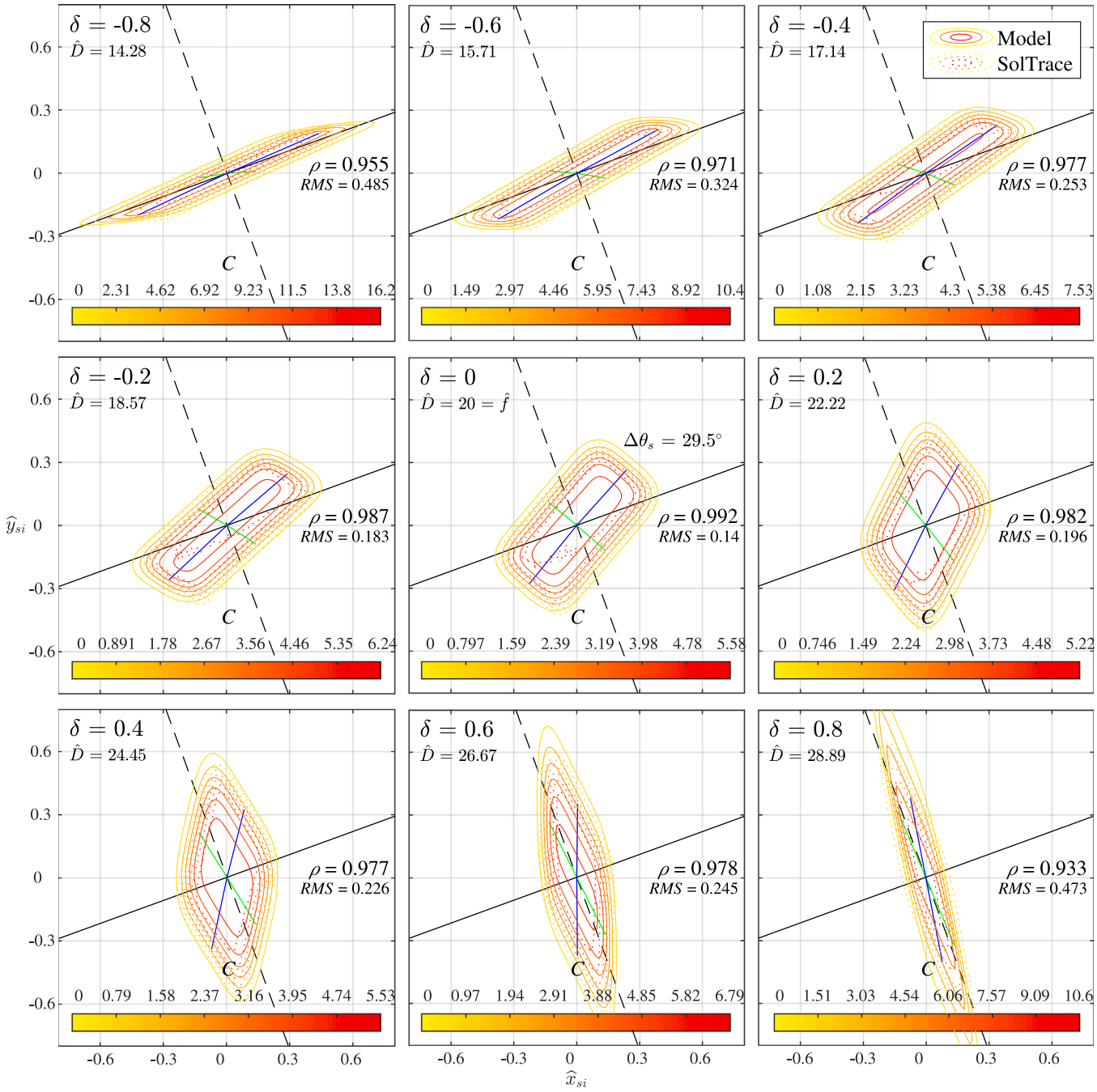

Fig. 8. Concentration maps in the image plane by the model (solid isolines) and SolTrace (dotted) for several δ relative distances. Angles: $\omega = 50°$, $\beta = 20°$. Mirror: $\hat{f} = 20$, $LW = 2 \cdot LH$. (For interpretation of the references to color in this figure legend, the reader is referred to the web version of this article.)

the legend in the top right. Circular markers and solid lines stand for the model, while triangles and dotted lines for UNIZAR. It is important to note that UNIZAR, as long as not considering defocus, essentially generates the same spot regardless of the slant range. Just a slight scaling effect is introduced by UNIZAR analytic function because of the presence of D in Eqs. (7) and (9), but shape orientation is kept constant. Because of the more elongated flux distributions caused by astigmatism, as shown in previous Subsection, spillage losses in defocused heliostats might be higher than expected by UNIZAR.

As can be seen in Fig. 10, UNIZAR outperforms the proposed model for small incidence angles of 10° and 20°, where astigmatism is minor. For $\omega = 30°$, the correlation coefficients by the model surpass UNIZAR, even though ρ_{mod} may decrease up to 70% near the astigmatic foci. For incidence angles larger than 30°, the correlation coefficient rarely drops below 90% for the model, except near the sagittal focus. On the contrary, ρ_{uz} worsens drastically both with ω and $|\delta|$.

Regarding β angle, the model behaves better (higher ρ) with tangential and sagittal axes nearer to image plane axes, i.e. β angles around 0° and 90°. Having a look at the case of $\omega = 70°$ and $\beta = 20°$ (Fig. 10), a noticeable drop in ρ_{mod} is found in comparison with the rest of β angles. This is attributed to the uncertainty on the dominant direction. As $\Delta\theta_s = 46.8°$, tangential direction is taken as dominant and the corresponding case in Eqs. (22), (23), (25), and (26) applies. Thus, the proposed model reproduces with lower accuracy the flux distributions for $\Delta\theta_s$ close to 45°.

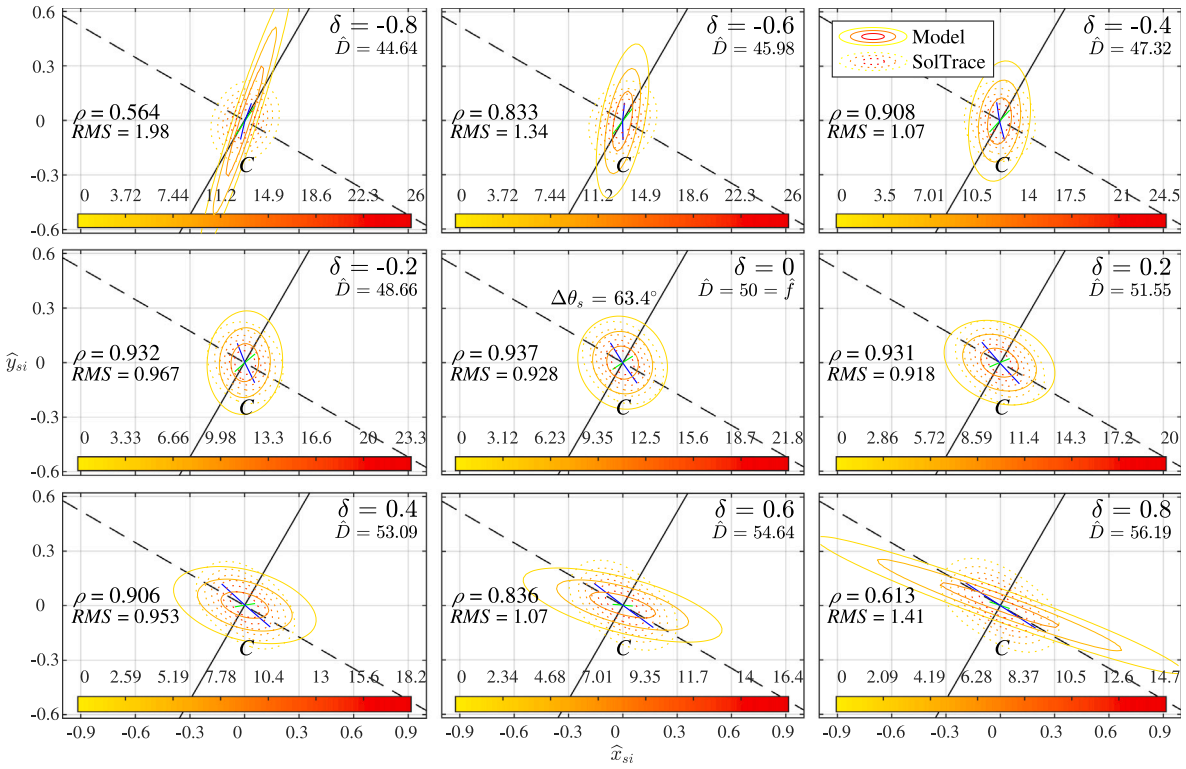

(a) $\omega = 30°$.

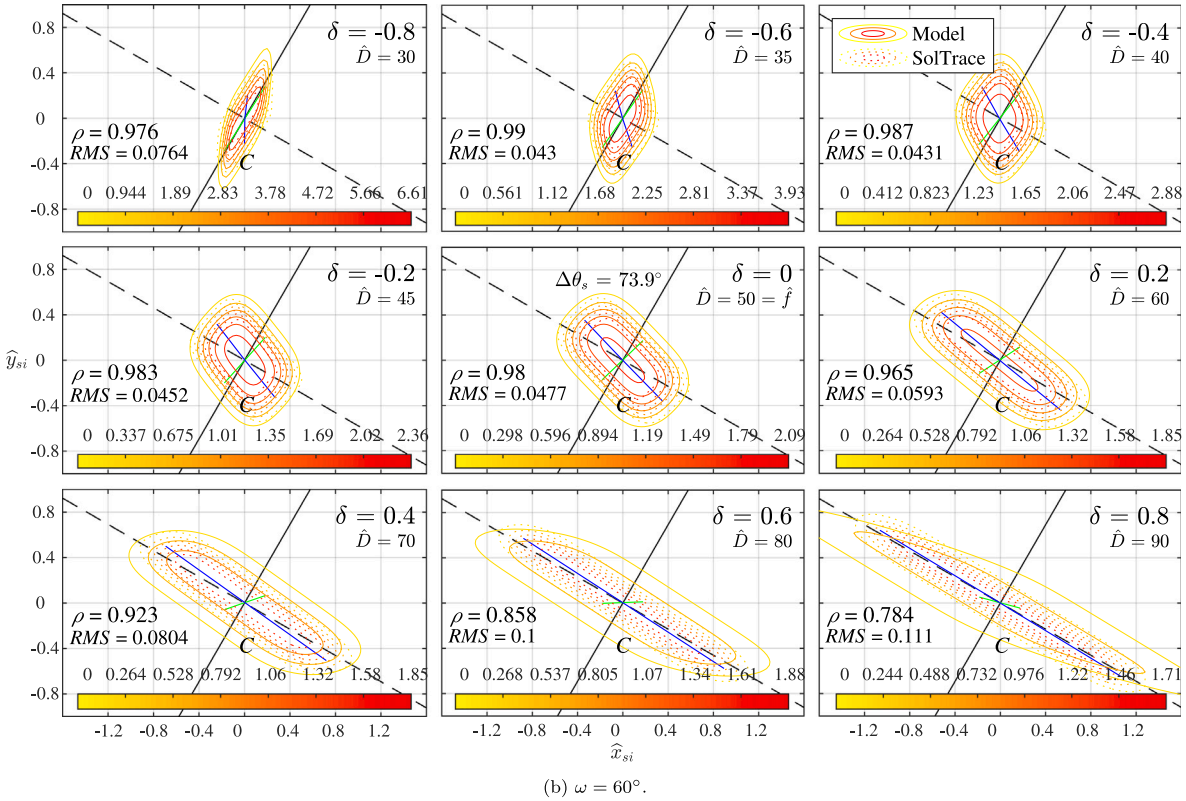

(b) $\omega = 60°$.

Fig. 9. Concentration maps in the image plane by the model (solid isolines) and SolTrace (dotted) for several δ relative distances ($\beta = 60°$). Mirror: $\hat{f} = 50$, $LW = 2 \cdot LH$. (For interpretation of the references to color in this figure legend, the reader is referred to the web version of this article.)

For $\hat{f} = 50$, Fig. 11 summarizes the correlation coefficients, both by the model and UNIZAR, with respect to MCRT results. UNIZAR outperforms the model for small incidence angles of 10° and 20°. For ω angles of 30° and 40°, UNIZAR starts decreasing the correlation coefficients but exceeds, except for $\beta = 0°$, those by the model, that clearly fails while approaching the astigmatic foci. For $\hat{f} = 50$, incidence angles might be above 40° in order to recommend the use of the model in comparison with UNIZAR. With $\omega \geq 50°$, the model

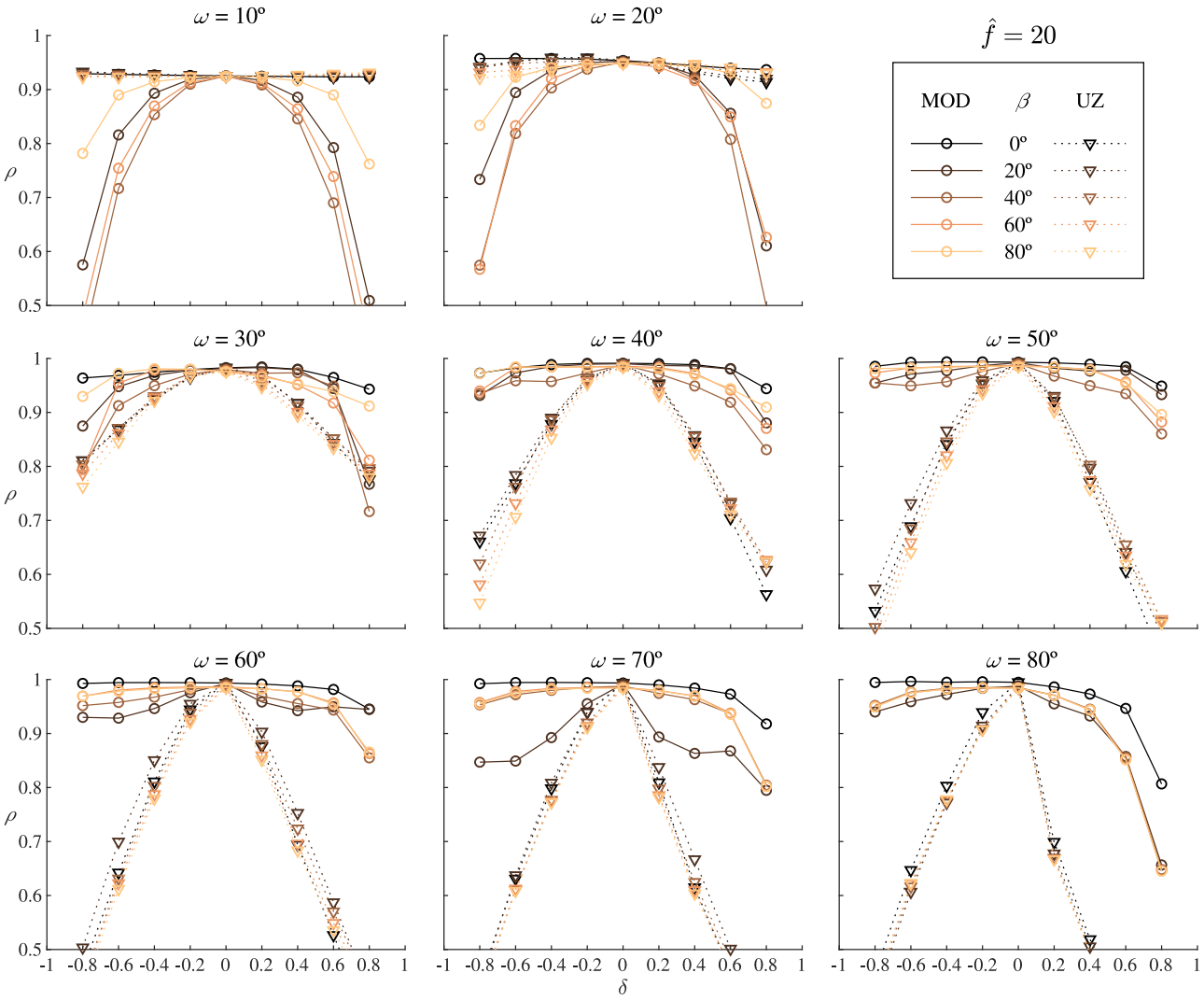

Fig. 10. For $\hat{f} = 20$, correlation coefficients by the MODEL and UNIZAR with respect to SolTrace depending on ω and δ. Mirror dimensions: $LW = 2 \cdot LH$. (For interpretation of the references to color in this figure legend, the reader is referred to the web version of this article.)

generally achieves correlation coefficients above 90%, except when approaching the sagittal focus. In fact, the higher the incidence angle is, the worse becomes the correlation coefficient towards the sagittal focus. Nonetheless, it is important to note that at high incidence angles, distances towards the sagittal focus (high δ) imply impractical long slant ranges, as can be deduced from Fig. 5.

Comparing the results for $\hat{f} = 20$ (Fig. 10) and $\hat{f} = 50$ (Fig. 11), two conclusions arise. First, the proposed and UNIZAR functions are complementary; in the event of severe astigmatism and defocus, the proposed model reproduces the spot aberrations. Secondly, the smaller the focal length of the reflector is, the wider becomes the range of incidence angles where the proposed model is more accurate.

Simulations for other focal lengths were carried out to confirm the second conclusion. From the analysis of simulation results, Fig. 12 shows in a ω vs. $\hat{f}$ graph the validity region for the proposed model in a light color.

The validity of the proposed model is therefore directly proportional to the incidence angle and inversely proportional to the focal length. Such a relationship is implicitly considering the combined effect of astigmatism and defocus. To quantify this effect, a parameter has been introduced with ω in the numerator and $\hat{f}$ in the denominator. Specifically, it has been found that the ratio $\sqrt{J_{uz}}/\hat{f}$ accounts reasonably well for the impact of astigmatism and defocus. High values of this parameter imply significant aberrations, and the other way round.

Contrasting the $\sqrt{J_{uz}}/\hat{f}$ parameter with the region of validity in Fig. 12, it turns out that a value of 0.005 establishes an advisable threshold to identify the regions of validity for the proposed model and UNIZAR. This model validity threshold is expressed in Eq. (30). Thus, the curved line separating both regions in Fig. 12 correspond to $\sqrt{J_{uz}}/\hat{f} = 0.005$.

$$\sqrt{J_{uz}}/\hat{f} = \frac{LH}{f}(1 - \cos\omega) > 0.005 \quad \text{(Model validity)} \tag{30}$$

For proper interpretation of the validity graph in Fig. 12, let us remind that $\hat{f}$ is the non-dimensional focal length with respect to the mirror height, taking advantage of the scaling property in SPT optical systems, with the exception of attenuation losses. Given a state-of-the-art field with heliostats of $LH = 10$ m, if the tower is 100 m high, the first rows of heliostats might have focal lengths of around $f = 150$ m, which is equivalent to $\hat{f} = 15$ (=150/10). Therefore, for such heliostats, the proposed analytic function works fine with incidence angles above around 20°. On the contrary, heliostats in the last rows might have focal lengths of around $f = 700$ m, i.e. $\hat{f} = 70$. In such a case, the proposed model is appropriate whether the incidence angles are above 50°.

6. Conclusions

An analytic function, that deals with defocus and astigmatism in single heliostats, has been developed. This analytic function is based on

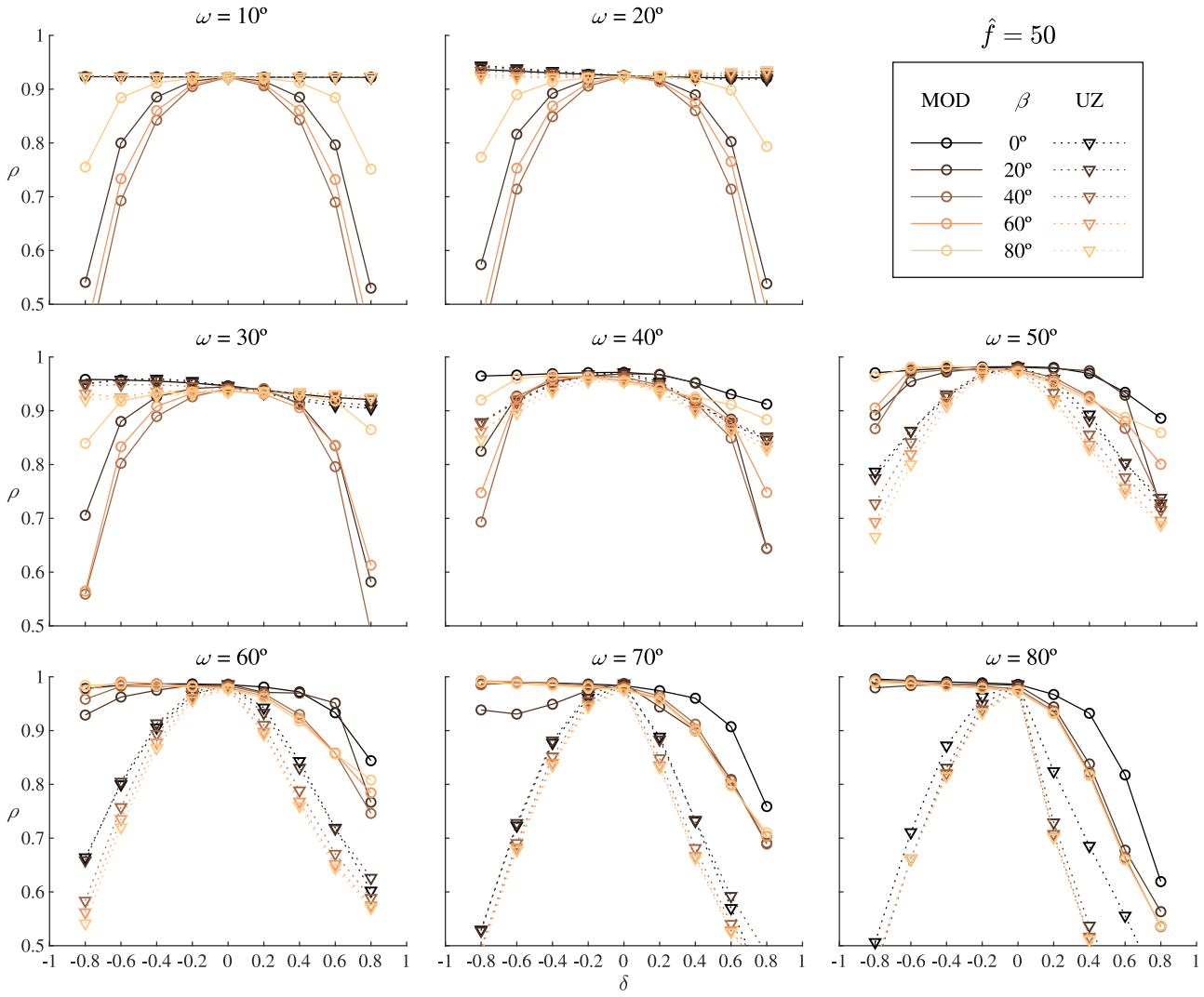

Fig. 11. For $\hat{f} = 50$, correlation coefficients by the MODEL and UNIZAR with respect to SolTrace depending on ω and δ. Mirror dimensions: $LW = 2 \cdot LH$. (For interpretation of the references to color in this figure legend, the reader is referred to the web version of this article.)

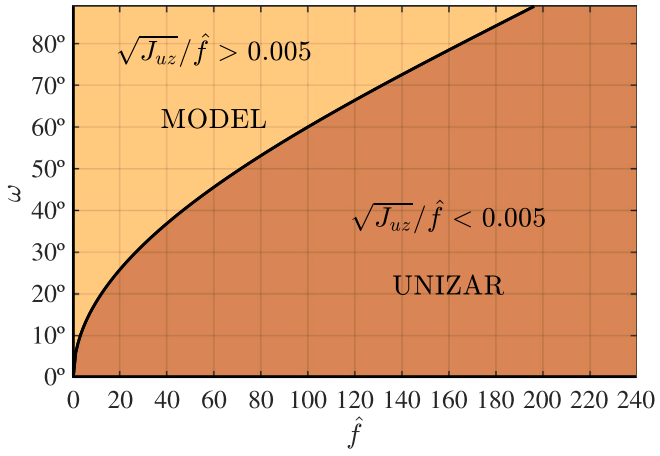

Fig. 12. Validity regions ($\hat{f} - \omega$ pairs) for the MODEL and UNIZAR, taking the astigmatic threshold: $\sqrt{J_{uz}}/\hat{f} = 0.005$.

UNIZAR one at the image plane and has been complemented with the astigmatism theory. Astigmatic aberrations have been detected when the incidence angle increases.

Under defocus –slant range different to the mirror focal length–, it has been found that the reflected heliostat axes are not perpendicular. The heliostat flux distribution shapes along these two non-orthogonal axes. The model resulting from the proposed analytic function, accounts for two rotation angles. The vector procedure to determine these θ_H and θ_V angles has been detailed in Appendix.

The analysis of flux maps has shown that the spot aligns along the sagittal direction at the tangential focus and, conversely, along the tangential direction at the sagittal focus. The definition of the analytic function is piecewise, depending on the dominant direction: tangential vs. sagittal. At the astigmatic foci, the proposed analytic function is indeterminate as both rotation angles are the same and $|\sin(\theta_H - \theta_V)|$, numerator in axis transformation, becomes zero.

Except for slant ranges near the tangential and the sagittal foci, the proposed model has been compared with MCRT simulations to assess its validity. When UNIZAR analytic function fails to reproduce the astigmatic phenomena under defocus, the proposed function has yielded cross-correlation coefficients above 90%. Results show that the proposed model is complementary to UNIZAR.

The parameter $(1 - \cos\omega)\, LH/f$ has been identified as a good indicator of the combined effect of astigmatism and defocus. When this

parameter surpasses 0.005, it has been found that the proposed model behaves better than the original UNIZAR. In terms of a heliostat field configuration, the proposed model outperforms for large heliostats, or small ones near the tower, whenever the incidence angle is high enough.

Because of the limited computational cost of analytic functions compared to MCRT, flux mapping with these simplified models is still advantageous in optimization studies. The proposed analytic function solves the distribution for defocus and severe astigmatism, but fails when the slant range approaches the astigmatic focal lengths, especially the sagittal focus. Hence, it is still pending a universal analytic function, accurate for any slant range and incidence angle.

Declaration of competing interest

The authors declare that they have no known competing financial interests or personal relationships that could have appeared to influence the work reported in this paper.

Acknowledgments

This work has been supported by the Madrid Government (Comunidad de Madrid), Spain under the Multiannual Agreement with UC3M in the line of "Fostering Young Doctors Research" (VISHELIO-CM-UC3M), and in the context of the V PRICIT (Regional Programme of Research and Technological Innovation). Funding for APC: Universidad Carlos III de Madrid (Read & Publish Agreement CRUE-CSIC 2022).

Appendix. Rotation angles

This Appendix describes the vector procedure to determine θ_H and θ_V angles. Bold letters denote 3D vectors, which are position vectors for uppercase letters.

Heliostat mirrors ideally have a spherical surface with R curvature radius equal to twice the focal length ($R = 2f$). In the heliostat system of coordinates (sh), the position vector of the mirror center ($\mathbf{O}_{sh}$) is set according to Eq. (A.1).

$$\mathbf{O}_{sh} = \begin{pmatrix} 0 & 0 & R \end{pmatrix} \tag{A.1}$$

As depicted in Fig. 3(b), the heliostat horizontal and vertical axes are reflected into the image plane. The angle between the heliostat reflected axes and the horizontal axis of the image plane determines θ rotation angles, as shown in the image plane views in Fig. 4.

For the horizontal axis of the heliostat, its endpoint is named **H**, as shown in Fig. 3(b). Being LW the heliostat width, $\mathbf{H}_{sh}$ position vector is set by Eq. (A.2).

$$\mathbf{H}_{sh} = \begin{pmatrix} LW/2 & 0 & 0 \end{pmatrix} \tag{A.2}$$

The normal unit vector of the heliostat at point **H** is computed with Eq. (A.3), on the basis of $\mathbf{O}_{sh}$ virtual center of the spherical mirror.

$$\mathbf{n}_{H,sh} = \frac{\mathbf{O}_{sh} - \mathbf{H}_{sh}}{\left|\mathbf{O}_{sh} - \mathbf{H}_{sh}\right|} \tag{A.3}$$

The main reflected ray at **H** follows Eq. (A.4), according to Snell's reflection law. Sun unit vector in the heliostat system of coordinates ($\mathbf{s}_{sh}$) results from its transformation from the global coordinate system (Eq. (A.5)). Rot_{g2h} is the 3 × 3 rotation matrix from global to heliostat coordinate systems. The construction of this rotation matrix has been detailed in (Sánchez-González and Santana, 2015).

$$\mathbf{r}_{H,sh} = 2\left(\mathbf{n}_{H,sh} \cdot \mathbf{s}_{sh}\right)\mathbf{n}_{H,sh} - \mathbf{s}_{sh} \tag{A.4}$$

$$\mathbf{s}_{sh} = Rot_{g2h} \cdot \mathbf{s}_{sg} \tag{A.5}$$

To transform $\mathbf{r}_H$ reflection vector at **H** from the heliostat (sh) to the image (si) system of coordinates, the 3D transformation in Eq. (A.6) applies. Rot_{h2i} rotation matrix comprises from Rot_{h2g} and Rot_{g2i} rotation matrices (Eq. (A.7)). The construction of the latter rotation matrix –global to image– has been described too in (Sánchez-González and Santana, 2015).

$$\mathbf{r}_{H,si} = Rot_{h2i} \cdot \mathbf{r}_{H,sh} \tag{A.6}$$

$$Rot_{h2i} = Rot_{g2i} \cdot Rot_{h2g} \tag{A.7}$$

Following Eq. (A.8), **H** position vector is transformed from heliostat to image coordinate system with Rot_{h2i} rotation matrix and $\begin{pmatrix} 0 & 0 & D \end{pmatrix}$ translation vector, D being the slant range.

$$\mathbf{H}_{si} = Rot_{h2i} \cdot \mathbf{H}_{sh} + \begin{pmatrix} 0 & 0 & D \end{pmatrix} \tag{A.8}$$

The reflection of **H** into the image plane ($\mathbf{H'}_{si}$) finally results from Eq. (A.9). The exact distance from **H** to its reflection (**H'**) is accounted for by the $z_{si}(\mathbf{H})/z_{si}(\mathbf{n}_H)$ term, that involves the z-coordinate of **H** and $\mathbf{r}_H$ vectors in the image coordinate system.

$$\mathbf{H'}_{si} = \mathbf{H}_{si} + \frac{z_{si}(\mathbf{H})}{z_{si}(\mathbf{r}_H)}\mathbf{r}_{H,si} \tag{A.9}$$

With the knowledge of $\mathbf{H'}_{si}$, position vector of the reflection in the image plane, the angle of the reflected heliostat horizontal axis (θ_H) is straightforward. In Matlab® environment, *cart2pol* function can be used. Alternatively, Eq. (A.10) determines such an angle, but the sign convention (positive counterclockwise) must be later applied.

$$\theta_H = \arccos\left(\frac{\mathbf{H'}_{si}}{\left|\mathbf{H'}_{si}\right|} \cdot \begin{pmatrix} 1 & 0 & 0 \end{pmatrix}\right) \tag{A.10}$$

For the vertical axis of the heliostat, the angle of its reflection on the image plane (θ_V) follows equivalent Eq. (A.11). Being **V** the endpoint of the vertical axis, its position vector in heliostat system of coordinates is set by Eq. (A.12). To obtain the reflection of **V** into the image plane, $\mathbf{V'}_{si}$, Eqs. (A.3) to (A.9) apply, while substituting **H** by **V**.

$$\theta_V = \arccos\left(\frac{\mathbf{V'}_{si}}{\left|\mathbf{V'}_{si}\right|} \cdot \begin{pmatrix} 1 & 0 & 0 \end{pmatrix}\right) \tag{A.11}$$

$$\mathbf{V}_{sh} = \begin{pmatrix} 0 & LH/2 & 0 \end{pmatrix} \tag{A.12}$$

References

Biggs, F., Vittitoe, C.N., 1979. Helios Model for the Optical Behavior of Reflecting Solar Concentrators. Technical Report, Sandia National Laboratories. SAND-76-0347, http://dx.doi.org/10.2172/6273705.

Buck, R., Teufel, E., 2009. Comparison and optimization of heliostat canting methods. J. Solar Energy Eng. 131 (1), 011001. http://dx.doi.org/10.1115/1.3027500.

Camacho, E.F., Berenguel, M., Rubio, F.R., Martínez, D., 2012. Control of central receiver systems. In: Advances in Industrial Control. pp. 239–313. http://dx.doi.org/10.1007/978-0-85729-916-1_6.

Chen, Y., Kribus, A., Lim, B., Lim, C., Chong, K., Karni, J., Buck, R., Pfahl, A., Bligh, T.P., 2004. Comparison of two sun tracking methods in the application of a heliostat field. J. Solar Energy Eng. 126 (1), 638. http://dx.doi.org/10.1115/1.1634583.

Coddington, H., 1825. An Elementary Treatise on Optics. J. Smith.

Collado, F.J., 2010. One-point fitting of the flux density produced by a heliostat. Sol. Energy 84 (4), 673–684. http://dx.doi.org/10.1016/j.solener.2010.01.019.

Collado, F.J., Gómez, A., Turégano, J., 1986. An analytic function for the flux density due to sunlight reflected from a heliostat. Sol. Energy 37 (3), 215–234. http://dx.doi.org/10.1016/0038-092X(86)90078-2.

Cruz, N., Redondo, J., Berenguel, M., Álvarez, J., Ortigosa, P., 2017. Review of software for optical analyzing and optimizing heliostat fields. Renew. Sustain. Energy Rev. 72, 1001–1018. http://dx.doi.org/10.1016/j.rser.2017.01.032.

Garcia, P., Ferrière, A., Bezian, J.-J., 2008. Codes for solar flux calculation dedicated to central receiver system applications: A comparative review. Sol. Energy 82 (3), 189–197. http://dx.doi.org/10.1016/j.solener.2007.08.004.

Hanrieder, N., Wilbert, S., Mancera-Guevara, D., Buck, R., Giuliano, S., Pitz-Paal, R., 2017. Atmospheric extinction in solar tower plants – a review. Sol. Energy 152, 193–207. http://dx.doi.org/10.1016/j.solener.2017.01.013.

Hénault, F., 2015. Fast computation of solar concentrating ratio in presence of opto-mechanical errors. Sol. Energy 112, 183–193. http://dx.doi.org/10.1016/j.solener.2014.12.002.

Igel, E., Hughes, R., 1979. Optical analysis of solar facility heliostats. Sol. Energy 22, 283–295. http://dx.doi.org/10.1016/0038-092X(79)90143-9.

Landman, W.A., Grobler, A., Gauché, P., Dinter, F., 2016. Incidence angle effects on circular Gaussian flux density distributions for heliostat imaging. Sol. Energy 126, 156–167. http://dx.doi.org/10.1016/j.solener.2015.12.008.

Lim, B.-H., Chong, K.-K., Lim, C.-S., Lai, A.-C., 2016. Latitude-orientated mode of non-imaging focusing heliostat using spinning-elevation tracking method. Sol. Energy 135, 253–264. http://dx.doi.org/10.1016/j.solener.2016.05.038.

Meng, L., You, Z., Arif, a.F.M., Dubowsky, S., 2013. Shape optimized heliostats using a tailored stiffness approach. J. Solar Energy Eng. 136 (2), 021017. http://dx.doi.org/10.1115/1.4025827.

Sánchez-González, A., Rodríguez-Sánchez, M.R., Santana, D., 2017. Aiming strategy model based on allowable flux densities for molten salt central receivers. Sol. Energy 157, 1130–1144. http://dx.doi.org/10.1016/j.solener.2015.12.055.

Sánchez-González, A., Santana, D., 2015. Solar flux distribution on central receivers: A projection method from analytic function. Renew. Energy 74, 576–587. http://dx.doi.org/10.1016/j.renene.2014.08.016.

Schwarzbözl, P., Schmitz, M., Pitz-paal, R., 2009. Visual HFLCAL — a software tool for layout and optimisation of heliostat fields. In: SolarPACES, Berlin, Germany. URL: https://elib.dlr.de/60308/.

Speetzen, N., Richter, P., 2021. Dynamic aiming strategy for central receiver systems. Renew. Energy 180, 55–67. http://dx.doi.org/10.1016/j.renene.2021.08.060.

Walzel, M.D., Lipps, F.W., Vant-Hull, L.L., 1977. A solar flux density calculation for a solar tower concentrator using a two-dimensional Hermite function expansion. Sol. Energy 19 (3), 239–253. http://dx.doi.org/10.1016/0038-092X(77)90067-6.

Wendelin, T., Dobos, A., Lewandowski, A., 2013. SolTrace: A Ray-Tracing Code for Complex Solar Optical Systems. Technical Report, NREL. National Renewable Energy Laboratory, Golden, Colorado, URL: http://www.nrel.gov/docs/fy14osti/59163.pdf.

Winter, C., Sizmann, R.L., Vant-Hull, L.L., 1991. Solar Power Plants. Fundamentals, Technology, Systems, Economics. Springer-Verlag, Heidelberg, http://dx.doi.org/10.1007/978-3-642-61245-9.

Zaibel, R., Dagan, E., Karni, J., Ries, H., 1995. An astigmatic corrected target-aligned heliostat for high concentration. Sol. Energy Mater. Sol. Cells 37, 191–202. http://dx.doi.org/10.1016/0927-0248(94)00206-1.